1D Nanomaterial-Based Highly Stretchable Strain Sensors for Human Movement Monitoring and Human–Robotic Interactive Systems

Abhishek Singh Dahiya, Thierry Gil, Jérôme Thireau, Nadine Azemard, Alain Lacampagne, Benoît Charlot, Aida Todri-Sanial

One-dimensional nanomaterial based highly stretchable strain sensors for human movement monitoring and human-robotic interactive systems

Abhishek Singh Dahiya[1], Thierry Gil[2], Jerome Thireau[3], Nadine Azemard[2], Alain Lacampagne[3], Benoit Charlot[4], Aida Todri-Sanial[2*]*

[1]Bendable Electronics and Sensing Technologies (BEST) group, James Watt School of Engineering, University of Glasgow G12 8QQ Glasgow, UK
[2]LIRMM, Université de Montpellier, CNRS, Montpellier, France
[3]PhyMedExp, Université de Montpellier, CNRS, INSERM, Montpellier, France
[4]IES, Université de Montpellier, CNRS, Montpellier, France

***Corresponding author(s) email: benoit.charlot@um2.fr; aida.todri@lirmm.fr**

Keywords

Stretchable piezoresistive strain sensors, one-dimensional materials, human movement detection, human-robotic interaction, soft robotics

Abstract

This paper describes a facile strategy of micromolding-in-capillary process to fabricate stretchable strain sensors wherein, the sensing material is wrapped within silicone rubber (Dragon Skin™ (DS)) to form a sandwich-like structure. Two different one-dimensional (1D) sensing materials have been exploited to fabricate and study strain sensing performance of such device structure, namely multi-walled carbon nanotubes (MWCNTs) and silver nanowires (Ag NWs). The fabricated strain sensors using MWCNT exhibits wide sensing range (2 - 180%), and moderately high sensing performance with outstanding durability (over 6000 cycles). It is found that MWCNT present a strong strain dependent character in the 45 to 120% elongation regime. On the other hand, very high gauge factor of > 10^6 is achieved using Ag NWs at 30% strain with good stability (over 100 cycles). Sensing mechanisms for both 1D conductive sensing materials is discussed. They can be applied for human motion monitoring such as finger, knee and wrist bending movements to enable human physiological parameters to be registered and analysed continuously. They are also employed in multichannel and interactive electronic system to be used as a control mechanism for teleoperation for robotic end-effectors.

The developed sensors have potential applications in health diagnosis and human-machine interaction.

1. Introduction

Wearable electronics have gained compelling interest because of the wide range of applications they enable such as health monitoring, diagnostics, and human–machine interfaces. Significant achievements have been made demonstrating variety of flexible electronic devices such as tattoo-like sensory skin patches[1–3], energy harvesters[4], energy storage elements[5,6], stretchable interconnects[7] etc. The astonishing progress in the technologies mentioned above have enabled a new technological drive called "Internet-of-Medical-Things (IoMT)", linking wearable devices/sensors into a communication network for real-time or periodic patient-doctor communications.[8] The IoMT will help people to better monitor their health status by collecting subtle vital signs modifications and transferring to healthcare service providers. Part of the on-going research efforts to develop IoMT is focused on the development of wearable sensors that can be embedded in clothing[9–11], wrist watches, patches[12] and bands[13–16], contact lenses[17–21], tattoo-like sensory skin patches (electronic-skin)[2,22] etc. to enable around-the-clock vital signs monitoring, human-machine interactive systems[2] and as bionic ligaments in soft robotics[23].

Among various types of wearable mechanical sensors such as piezoresistive, piezoelectric and capacitive, the piezoresistive-based strain sensors are gaining a lot of interest as they provide high sensitivity with simple device design and readout circuits[24–30] for vital signs monitoring and soft robotics. Piezoresistive strain sensors are based on the change of electrical properties of the material when subjected to mechanical deformation. Piezoresistive sensor is often named as a resistive strain sensor or simply strain gauge, are widely used in measuring strain, tension and acceleration. Simplest of the resistive strain sensors are metal strain gauges. Typically, they are a meander shaped metal wire patterned on a flexible polyimide film and sensitive to

bending[31,32] (detection limit of <5%). The sensitivity or gauge factor (GF) - defined as the rate of relative change in electrical resistance to mechanical strain - of such devices is low with typical values between 1-5[32]. To improve the sensitivity of metal based stretchable strain sensors, microcracking of the metallic thin-films has shown promising results[33,34]. For example, Kang et al. reported on nanoscale crack junctions in Platinum (Pt) metal thin films, inspired by the crack-shaped slit sensory organs of spiders, with very high sensitivity[33]. A GF of 2000 over a range of 0–2% is achieved, allowing for detection of physiological signals such as speech patterns and heart rate. However, the durability and stretchability of such a device is limited, showing signal degradation after about 500 cycles of 2% strain, i.e. barely ten minutes of continuous heart rate monitoring in humans. The microcracking-based approach can yield high GF, but device stability remains a big issue to be resolved.

The important requirements for resistive strain sensors to be employed for wearable applications are: (i) high flexibility and stretchability to absorb strain with body movements, (ii) compactness and small size, (iii) high sensitivity, (iv) biocompatibility, and (v) insensitivity to biological fluid such as sweat. To address this issue, a new class of materials called 'nanocomposite (NC) materials' are being investigated[35–39]. This new class of material is a mixture of viscoelastic polymer matrix (organic) and conductive fillers (inorganic) and have the potential to fulfil the requirements of wearable mechanical strain sensors. These conductive polymer composite materials can be realized using carbonaceous nanomaterials (e.g. carbon nanotubes (CNTs)[38–44], graphene[45]), inorganic metallic nanomaterials (e.g., silver nanowires[37,46], and nanoparticles[47]), hydrogels[48,49], etc. for body motion detection. This class of material is unique as it retains many desirable features of polymers (flexibility, biocompatibility, processability) and provide opportunities to control the electrical properties of the NC such as permittivity[50–54], through the amount of added filler material. Based on the percolation theory[55], NCs can achieve an insulator/conductor transition when the filler content

is high enough to build up the percolated conductive networks throughout the polymer matrix [51]. Among variety of filler materials investigated, one-dimensional (1D) conductive nanomaterial, such as carbon nanotubes (CNTs)[38–44] and metallic nanowires (NWs)[37,46], have drawn significant interest to realize NC for strain sensing applications. Interest in CNTs has been mainly driven because of its excellent mechanical properties, chemical inertness, and low cost. For instance, CNT based NCs stretchability could reach up to 500%. On the other hand, metallic nanomaterials can provide high sensitivity due to better electrical properties compared to CNTs. Using metal nanostructures, high GF is easily achieved such as more than two times than with CNTs [23]. Amongst the list of metals, silver (Ag) based nanomaterials are most exploited for the development of NC based strain sensors. This can be attributed to its good electrical (highest room-temperature electrical conductivity) and physical properties (resistant to oxidation)[46,56]. Copper (Cu) NWs has also gained importance because of its high conductivity (6% less than that of Ag) and is much cheaper. However, fast oxidation of Cu metal limit its use as a conductive filler material[7,57].

Extensive research efforts have been conducted on the development of dispersion methods of filler material to have uniform dispersion into the polymer matrix to reduce the amount of filler material and also improve NC conductivity[40,58]. Typically, the filler content is at least 1-2% of the hybrid network, which is still very high. Research efforts are on-going to develop alternative fabrication approaches to further reduce the amount of filler material and thus, decrease the cost and complexity of the fabrication process. Innovative fabrication approaches have been experimented to develop highly sensitive resistive sensors employing NC materials with pre-stretching[59], 3D printing[60], direct ink writing[61] and microfluidic techniques[27,62]. For instance, Muth et al., used 3D printing to fabricate sensitive strain sensors with conductive carbon grease materials to obtain a high stretchability of 400%.[60] It is challenging to design a high sensitivity strain sensor with improved stretchability. Ideally, a sensing device should

have a large stretchability as well as a high GF to measure the change in the electrical resistance upon deformation. More recently, an innovative yet simple device fabrication approach is reported to show an enhanced strain sensing performance. In this fabrication approach, networks of 1D materials, such as CNTs or silver (Ag) nanowires (NWs), on top of a stretchable substrate are realized in a micro/macro channels, which offers an alternative way to realize stretchable strain sensors with high GF[23,27]. Using this fabrication strategy, Han et al.,[23] created a NW-based strain sensor by hybridizing brittle metal nanowires (Ag NWs, Copper NWs, or CNTs) and a conductive organic solution with poly(3,4-ethylenedioxythiophene):polystyrene sulfonate (PEDOT:PSS). Nanowire microfluidic hybrid (NMH) strain sensors exhibit record-high values for both GF and stretchability. This is because the advantages of both materials have been coupled. The brittleness of the NWs endows the strain sensor with an outstanding sensitivity under a small stretchable load, and the conductive organic solution significantly enhances the deformation endurance of the device. However, not all these technologies can be used to manufacture strain sensors at low cost with all desired characteristics - high stretchability, excellent gauge factor, low-power consumption, linear response and impressive repeatability and stability.

In this work, we present a new, facile and cost-effective strategy by exploiting micromolding-in-capillary (MIMIC) process to construct organic/inorganic hybrid nanocomposite based stretchable strain sensors, the sensing material i.e. 1D nanomaterial is wrapped within dragon-skin (DS) polymer to form a sandwich-like structure. The unique advantages of the developed fabrication process are the use of significantly less amount of filler material to obtain high NC conductivity as compared to conventional NC materials. Secondly, we obtain excellent dispersal of filler material in polymer matrix without any chemical or physical treatment. The stretchable strain sensors showed superior performance device characteristics such as high sensitivity, excellent durability and wide strain sensing range (strain sensitivity between 2-

200%). We describe the strain sensing mechanisms based on the quantitative investigations we performed on the developed sensors. The sensors are employed to monitor subtle and large human body movements such as finger, wrist, artificial knee joint, and respiratory movements. The MWCNT/DS sensors are also employed in multichannel and interactive electronic system to be used as a control mechanism for teleoperation for robotic end-effectors.

2. Results and discussions

2.1 Strain sensor fabrication process

The fabrication method of strain sensors is inspired from a micromolding-in-capillary (MIMIC)[63] process, schematically shown in the **Figure 1a**. In the first step, the grooved bottom dragon-skin (DS) plate is realized using a standard molding process. The groove dimensions and depth can be tuned according to the size and thickness of polyimide or SU-8 (epoxy-based negative photoresist) layer. For example, a feature size of 100 µm is obtained using a standard photolithography process employing SU-8 negative resist (**Figure S1**) whereas macro-size features are developed using standard polyimide Kapton tape. Next, a drop of the 1D material suspension (approximately 100µL) is introduced at the DS mold tip. The suspension filled the channels of the DS mold through capillary forces. In the MIMIC process, the rate of capillary filling depends on the kinematic viscosity, surface tension of the liquid, and section size of the capillary.[63,64] To improve the wettability of 1D material suspension to the DS, a 90s oxygen plasma treatment is carried out before dropping the suspension. In the third step, copper (Cu) wires are attached using silver epoxy paste. In the last step, "sandwich" structure is realized by pouring another layer of DS which flows into the 1D connected network and cross-linked with the bottom layer of DS (realized in step 1). The top DS layer will fully and firmly encapsulate the 1D sensing material, and thus improve the robustness of the device. The cross-sectional scanning electron microscopy (SEM) images of the packaged 1D sensing

material, between two DS layers, is shown in the **Figure 1b**. From SEM images, an interconnected percolated network of 1D sensing material is formed, and firmly encapsulated within DS polymer.

There are two important and interesting features of the developed MIMIC fabrication process. First, 1D material is uniformly percolated within DS polymer, a feature difficult to obtain in conventional organic/inorganic composite materials.[65] Generally, disentanglement procedure is needed when dry CNTs are dispersed in a polymeric medium. So far, most of research is focused on the development of disentanglement/alignment methods of CNTs. There are diverse chemical and physical methods to disperse CNTs.[40] However, the entangled CNTs require quite a long time to be wetted especially when CNTs are in contact with an incompatible fluid. Moreover, the CNT surface is modified to ensure chemical compatibility between CNTs and the matrix. It is important to note that, in our fabrication method, no such physical or chemical pre-treatment was performed to disperse MWCNTs and/or AgNWs.

Second, organic/inorganic based NCs can achieve an insulator/conductor transition when the filler content is high enough to build up the percolated conductive networks throughout the polymer matrix.[42] In our fabrication approach, the amount of filler material is negligible compared to the organic part (100-200µL of 0.5wt% MWCNTs in IPA and 100-200µL of 5mg/ml AgNWs in ethanol). **Figure 1c** presents the bar graph showing average nominal resistance values obtained using MWCNTs and Ag NWs sensing material. As expected, Ag NWs / DS NC material exhibit lower resistance values (~100 Ω) compared to MWCNT / DS NC (~1 kΩ).

2.2 Electromechanical performance of the stretchable strain sensors

The electromechanical properties of the developed strain sensors are characterized in detail using our custom-built test bench, as shown in the **Figure 2a**. The MWCNT/DS strain sensors are tested under uniaxial strains, and the electrical responses are characterized by the variations

in the relative responses, $\Delta r / r_0 = (r - r_0)/r_0$, where r_0 and r correspond to the original resistance and the real-time resistance under stretching, respectively. The sensitivity is quantified by calculating a figure of merit, i.e. the GF, which is defined as $GF = (\Delta r/r_0) / (\Delta l/l_0)$, where Δl is the change in the length and l_0 is the initial length. **Figure 2b** shows the variation of $\Delta r / r_0$, and GF with uniaxial stretching and release of the device. The graph shows that at small strain levels of up to 45% (i.e. 4.5 mm of stretching), the device showed an almost linear change of resistance with strain applied. At this strain level, the GF of the device remains between 3-5. Beyond 45% strain, the GF increases rapidly to reach around 60 at 120% strain. It is to note that the device showed no further increase in resistance and thus, GF of the sensor decreases beyond 120% strain to 40 at 180% strain level. When unloaded to zero strain level, the resistance comes back to the nominal value showing good recoverability. The nonlinear electromechanical behaviour of MWCNT/DS NC sensor can be explained by the discrete deformation behaviour of the filler networks at different strain regimes[66]. The strain dependent sensing mechanism is discussed in the later part of the manuscript.

Besides strain sensitivity, other important parameters to characterize in these NC materials are hysteresis or recoverability[67], response and relaxation times[23,42], environmental stability[68], linear response range[69], and repeatability.[68,69] From **Figure 2b**, we can see that the device showed a linear response up to 45% strain. We perform detailed sensor characterization when sensor is working in the linear regime with maximum applied strain of 40%. **Figure 2c** shows the optical images of the device at 0% percent strain (unstretched) and at 30% strain (loaded).

NC based strain sensors show hysteresis phenomenon. The electrical resistance of CNT NC films has been found to increase with increasing strain but remains almost constant as strain is released, forming a hysteresis between loading and unloading.[67] Ideally, there must be no hysteresis. To extract the magnitude of hysteresis in MWCNT/DS sensors, loading and unloading is performed using the test bench shown in **Figure 2a**. **Figure 3a** shows the

measured resistance, r as a function of the strain in the stretching (x) direction. The stretching is done periodically with the step of 0.2mm up to 3mm (30% strain) followed by the unloading of the device with similar step size to zero strain. **Figure 3b** shows the measured resistance values at each loading and unloading step. Upon unloading, the nominal resistance does not come back to the initial value and there exist significant amount of hysteresis in the device (~150Ω). The extracted $\Delta r/r_0$ values, using the data of **Figure 3b,** are shown in the **Figure S2.** The microstructural origin of this strain dependence remains unclear; however, some reports suggest that it is due to the irrecoverable loss of junctions between nanotubes while loading and unloading.[67,70] Zhang et al.[41] studied the strain sensing behavior of elastomeric composite films containing CNTs under cyclic loading. They reported that the important parameters to be studied to understand hysteresis issues are the testing strain rate and the molecular structure (e.g. hard segments vs. soft segments, degree of cross-linking, etc.). Although noticeable hysteresis exists after the first loading-unloading cycle, it is important to mention here that the sensor response is highly repeatable after the first loading cycle. The stability and robustness test results are shown in the subsequent section.

Nevertheless, we study the recoverability or hysteresis of strain sensor by recording the real-time response for repeated stretching-releasing cycles at a constant 30% strain and varying strain rate. The strain rate is varied from 0.01 mm/s to 10 mm/s with a step increase of one order. **Figure 3c** presents $\Delta r/r_0$ values when the strain sensor was stretched with different strain rates. Devices showed good recoverability and thus, less hysteresis at lower strain rate (even during the first loading cycle). For example, at the strain rate of 0.01 mm/s, the device showed almost zero hysteresis and complete recoverability. With increased strain rate (≥ 1mm/s), the device showed poor recoverability during the first stretch-release cycle but showed a stable response for the later loading-unloading cycles.

It is important to note that at higher strain rates, inconstancy in resistance change appears during the unloading process which resulted in the appearance of a 'shoulder peak' during cyclic loading, as shown in the Figure 3c. This phenomenon has been observed in other CNT/polymer composites, which is mainly attributed to the competition between the destruction and reconstruction of conductive networks during cyclic loadings.[41,42,71] The present investigation showed that such a shoulder peak can be removed at lower strain rates (< 0.1 mm/s). Further, we also observed that the appearance of shoulder peak is more distinct at higher strain values (**Figure S3**).

In addition to sensitivity and recoverability, strain sensors must have a fast response speed and recovery time. The response time is defined as the time interval required by the output signal of a sensor to rise 90% of the change in output signal when subjected to an input stimulus. As shown in the **Figure 3d**, it is the time delayed change in output signal for a step-like change in strain. The response time is extracted using the data shown in the **Figure 3c** and re-plotted in **Figure 3e** to show the sensor response time. It is to note that the $\Delta r/r_0$ values has been offset in y-axis for strain rate of 0.1, 1 and 10 mm/s. As expected, the response time is dependent on the rate of the strain applied. Faster response times are obtained when the device is stretched at higher strain rates. For instance, the sensor showed rapid response of less than 1 s when the strain rate is 10 mm/s. Whereas, when the sensor is strained to a slower rate of 0.01 mm/s, the sensor showed a response time of 150 s. The recovery time of the sensor is more than 150 s for the strain rate of 0.01 mm/s. To examine the strain sensing performance or sensitivity at different strains, $\Delta r/r_0$ in different cycles with stepwise increase in strain value is shown in **Figure 3f**. The sensor showed large working window, with detectable strain of as low as 2% to more than 50%. The $\Delta r/r_0$ value increases from 0.01 to almost 2 when 2% to 64% strain is applied.

Further, we studied the durability of the MWCNT/DS NC-based strain sensors by loading and unloading stretching cycles under two different loading conditions: (i) strain of 30% (900 stretch cycles at a strain rate of 0.1 mm/s), and (ii) 40% (6000 stretch cycles at a rate of 5 mm/s), as shown in **Figure 3g** and **3h**, respectively. In the beginning, the value of $\Delta r/r_0$ does not reach to its initial value, which is because some CNTs cannot return to their original places to rebuild the destroyed networks during the releasing process. For example, once the entanglements of CNTs are destroyed by stretching, they may never or takes long time to recover under releasing. After the first stretching-releasing cycles, however, it is observed that the maximum value of $\Delta r/r_0$ remains unchanged with the cycle number. This is because the conductive networks gradually reach a new equilibrium state. These results show that MWCNT/DS composite possess superior stability and repeatability, which could be used as smart strain sensors to continuously monitor human movements.

The MWCNT/DS nanocomposite-based sensor showed superior stability and durability, but the sensitivity is not as high as some of the reported values using other nanomaterials. An alternative to CNTs, metallic nanomaterials have good electrical properties and high sensitivity (GF is easily achieved twice or even more times than CNTs).[56,72] Therefore, to improve the sensitivity of the sensors, silver nanowires (Ag NWs) have been exploited using the similar MIMIC fabrication process. The fabrication process is exactly similar as shown in **Figure 1a**. The electromechanical properties of the developed AgNW/DS NC strain sensors are subsequently characterized, and the results are shown in **Figure 4**. **Figure 4a** shows the real-time resistance of the sensor when subjected to step wise strain increase. As it can be seen from this figure, the set compliance value (100V) is reached when sensor stretched to 1.6mm (corresponding strain is 16%). The applied current is 1µA. This corresponds to an open circuit condition where the flow of electrons is completely perturbed, and no flow of current exists between two silver electrodes. The sensor is further tested at two different strain rates: 0.1mm/s

(**Figure 4b**) and 1mm/s (**Figure 4d**). For both cases, strain is varied between 0 and 20%. **Figure 4c** shows the optical images of the device when stretch to 20% and when released back to 0% strain. A similar device performance is obtained for both strain rates with GF of 10^6, negligible hysteresis, fast response time and excellent recoverability. **Figure 4e-g** presents the durability test results for the AgNWs/DS NC sensor. The data show that for over 100 stretch-release cycles, the sensor performance is stable and shows no change in the initial resistance value. The change in resistance ($\Delta r/r_0$) and GF reached to a record high value of ~10^6 at small strain of 20% (**Figure 4h-i**).

To better assess the advantages and limitations of both NC types, i.e. MWCNT/DS and AgNW/DS, a performance comparison is made based on strain sensitivity, hysteresis or recoverability, response time, linear response range, and robustness as a function of applied strain rate. The detailed electromechanical characterization and results analysis for both NC types are summarized in **Table 1**. In terms of the sensitivity of the strain sensors, the AgNWs/DS NC showed a remarkable response. The obtained GF of more than 10^6 at 30% strain is one of the highest reported in the literature[47]. As it can be seen from the Table 1, ultrahigh GF of 10^7 has been achieved using Ag nanoparticles. However, sensing function for Ag based highly sensitive sensors is limited within a very narrow range. Undoubtedly, this strain sensor cannot monitor the external stimuli with large strain. On the other hand, MWCNT/DS NC based sensors displayed high robustness (6000 cycles tested) with moderately high sensitivity (GF between 3-60) and high sensing window (2-180%). Both NC types showed high stability at ambient conditions, fast response time at higher strain rates and negligible hysteresis after first loading-unloading cycle.

2.3 Sensing mechanisms

Based on our detailed electromechanical characterization and results analysis, we present the hypothesis on the working mechanisms of both sensor in **Figure 5**. The repeatable destruction

and reconstruction of the 2D or 3D scaffolds in 1D nanomaterials during cyclic loadings of the electrically conductive pathways inside the stretchable polymer matrix is the theoretical basis of NC-based stretchable strain sensors[35]. According to the literature, the physical contact between two nanomaterials (i.e. between MWCNTs) and their resulting tunnelling current are the two main factors to establish the sensing mechanisms on NC-based stretchable strain sensors. In other words, the current paths change during the stretch and release cycles due to change of connections between 1D nanomaterials.[73]

Ideally, the total resistance of an NC-based strain sensor is the sum of four types of resistances in series namely: contact resistance between metallic interconnects and NC (R_C); dimensional resistance (R_D); internal resistance of the nanomaterial (R_I); and tunneling resistance at the interconnection nodes of nanomaterial (R_T).[8] The device sensitivity is dictated by the change in total resistance with the applied strain. Generally, for a CNT based NC with good robustness, there is negligible change in the first three resistances i.e. R_C, R_D and R_I with applied strain thus, they can be omitted to explain the device working mechanism.[8] Therefore, the sensitivity of the strain sensor is dictated by the number and quality of interconnection nodes between 1D nanomaterial, dynamic (time-dependent) change of physical contact between them, and the tunnelling current. When a uniaxial tensile strain is applied to the nanocomposite, 1D material filaments (i.e. MWCNTs) are separated apart, leading to loss of contact points and widening of their distances. This impedes the current path (or the electron transferring ability of the conductive network) and causes the overall resistance to rise. Similarly, when NC is relaxed, the electron conduction paths are restored; therefore, the resistance drops with decreasing strain. The increase of the tunnel distance and the destruction of conductive paths lead to a significant increase in the electrical resistance of NCs during the stretching process.

The sensing mechanism on MWCNT/DS NC sensor is mainly due to the change on MWCNT network (destructions and reconstructions of conductive current paths) during cyclic loadings.

As shown in **Figure 5a**, before stretching, the sensor consists many conductive paths (because of tunnelling between two MWCNTs) between electrodes (marked with red colour paths). During stretching process, many of these conductive paths change (such as connections break and some new connections are made) leading to the change on sensor resistance. At the stretched position, reconstruction of the conductive paths begins, and new equilibrium state is reached. In our study, we find that the destruction and reconstruction of conductive networks is strongly dependent on the rate of applied strain (a dynamic phenomenon). Although the sensor response was highly repeatable after the first loading cycle, even at higher strain rate, there was noticeable hysteresis exists during the first loading-unloading cycle, as mentioned in **Table 1**. At the maximum stretched position, when the sensor is stretched with the highest strain rate (see **Figure 3c**), there are two 'shoulder' peaks. The first one is easy to understand. It arises at maximum stretched position because the conductive network starts to reconstruct itself and thus, resistance decreases a little. However, the appearance of the second peak is not clearly understood. We believe that during the release of the sensor (from maximum stretched position), the resistance of the sensor first increases, hinting the destruction of the quasi-stable state at the stretched position and then start to decrease to reach its initial state. Nevertheless, further studies are needed to confirm the origin of the second shoulder peak.

In this section, we will discuss the underlining mechanism responsible to achieve ultra-high GF using Ag NWs. The crack formation in metallic films is usually undesired as it leads to the device failure. However, it can be a very effective approach for achieving ultra-high GF if cracks can be controlled. It is well known that cracks can be easily induced in brittle metal films such as Ag, Pt, etc. due to the films' extremely low fracture toughness. Using strain induced crack approach, GF of 10^7 has been achieved using brittle Ag nanoparticles[47]. The occurrence and propagation of cracks in the concentrated strained areas of the brittle conductive layers is the proposed working mechanism for showing high sensitivity when using Ag

nanomaterial as filler material.[35] The appearance and propagation of the cracks lead to a remarkable increase in the electrical resistance. In this work, we have used Ag NWs which are expected to absorb more strain compared to thin films and nanoparticles (due to high surface-to-volume ratio). During the release process, the cracks on the conductive layer can be reconnected, thus causing the drop of the electrical resistance. On the other hand, MWCNTs have exceptional mechanical properties such as extreme tensile strength and Young's modulus. This is the reason that MWCNT/DS composite have shown more robust performance but at comparatively lower GF.

The AgNWs/DS based NC sensor operational mechanism is discussed with the help of the schematic shown in **Figure 5b**. Before stretching, the surface of the AgNW film is continuous (see the optical image in **Figure 4c**), and the conductive network is well integrated. When stretched, lots of cracks appeared in the AgNW film under a tensile strain of 20%. Many of the cracks are straight and almost across the entire width, indicating the brittle nature of AgNW interconnected network (optical image in **Figure 4c**). The occurrence of these cracks induces a drastic change in the device's electrical resistance, as shown in **Figure 4**, where a strong dependence of $\Delta r / r_0$ on r can be found.

2.4 Applications for Human Motion Detection

Human body deformations can be roughly divided into three regimes: small-scale (<5%); middle-scale (5–50%), and large-scale (50–100%).[23] When the strain is beyond 100%, the regime can be used for soft robotics.[23] As MWCNT/DS composite shows a large working window (stretchable up to 180%), it can be a promising platform for application as sensitive stretchable strain sensors for human and soft robots motion detection. Subsequently, as a proof-of-concept demonstration, we used the MWCNT/DS sensor to monitor the bending motion of the human body and artificial prosthetics. To monitor the finger movements, the device is mounted on a nitrile glove that is subsequently worn by a volunteer (**Figure 6a**). As presented

in **Figure 6a**, unambiguous stepwise resistance changes are recorded while the finger is bent gradually. The $\Delta r / r_0$ value increases from ~1.5 to 3 when bended at 45° and 90°, respectively (**movie#1**). Next, the sensor is mounted on a knee skeleton model to simulate ligament movement as shown in **Figure 6b**. When the skeleton model is bent to imitate human knee activity, the resistance variation gradually increases as the bending angle increases. The sensor showed a linear increase in resistance change with stepwise increase on the bending angle (with step of 5°). The device is capable to detect and discriminate the motions of a human leg, such as walking, running, and squatting based on the frequency and amplitude of the movement. To monitor wrist movements, the sensor is mounted on a nitrile glove that is subsequently worn by a volunteer. With slight changes in the wrist angle (~20°), the device shows detectable amount of resistance change. All the above proof-of-concept demonstration were made for medium to large deformation. Next, the sensor is mounted onto human skin to monitor subtle human activities, such as respiration. Respiration monitoring results during normal and deep breathing are shown in **Figure 6d**. The device showed detectable signals when the volunteer changes breathing rhythm from normal to deep. However, when monitoring respiration, the noise level is higher compared to when monitoring larger movements. The noises may be caused by the poor contact with the skin surface due to poor adhesion of the dragon-skin to skin. Efforts are underway to improve the adhesion of DS with human-skin.

Finally, the strain sensor is mounted on a nitrile glove (on index finger) and connected to a single-board microcontroller (Arduino UNO) and light emitting diodes (LEDs), as shown in the **Figure 7a** and **7b**. The microcontroller is programmed to light LEDs when strain sensor resistance increases. The resistance of the strain sensor is measured with a voltage divider circuit (**Figure 7c**). When the finger is bended and sensor is stretched, its resistance increases. The voltage at the terminals of the resistive sensor is measured through an analog-to-digital converter. The greater the resistance, the greater the voltage measured at the terminals and the

greater the number of illuminated LEDs (**movie#2**). Human motion detection is just one example of future applications. Due to the excellent stretchability and sensitivity, we believe MWCNT/DS sensor may also see a wide range of applications in structural damage diagnosis, humanoid robots, human-robot interaction and so on.

As a proof of concept device for human-robot interaction application, we have shown that MWCNT/DS sensors are sensitive enough to be used as a control mechanism for teleoperation for robotic end-effectors. The four developed strain sensors were attached on a commercially available glove. They were placed on the proximal interphalangeal (PIP) joints of the index, middle, ring and little fingers of the hand (**Figure 7d**). A simple voltage divider circuit measured the resistances of each individual sensor. The voltage divider outputs related to the analogue inputs of a microcontroller to be converted to digital data. Those data then were used to control the position of the servo motors attached to the robotic hand. At the same time, the microcontroller was connected to a custom-made LabVIEW program that was receiving the data from the controller and displayed the relative resistance of each sensor as seen in **Figure 7d**. As shown in **Figure 7e** and the **movie#3**, multichannel sensing and dynamic controlling were successfully demonstrated, indicating good feasibility of the MWCNT/DS stretchable sensors in human–robot interactive systems.

3. Conclusions

In summary, we proposed a simple and cost-effective fabrication process to produce sensitive and stretchable strain sensors for multiscale sensing. The strain sensors include macro channels filled with one-dimensional inorganic materials (MWCNTs or AgNWs) and organic silicone polymer. The organic/inorganic hybrid sandwich structure provides percolation paths for electrical conduction at the cost of a significantly low amount of filler material. The hybrid NC based sensor showed excellent performance with good sensitivity, excellent durability, negligible hysteresis and large working window to sense small-scale strain to large

deformation. Sensing mechanisms for both NCs, i.e. MWCNTs/DS and AgNWs/DS were described and presented using the quantitative characterization data. Sensors were tested to demonstrate real-world applications such as monitoring human body, artificial prosthetic movements, and human-machine interfaces. Using a single-board microcontroller, we have demonstrated changes in LEDs colours with the applied strain (no colour at zero strain, yellow at a lower level of strain and red colour at higher values of strain). Further, multichannel sensing and dynamic controlling were successfully demonstrated, indicating good feasibility of the MWCNT/DS stretchable sensors in human–robot interactive systems. This organic/inorganic hybrid strain sensor may advance the realization of future soft electronic devices, such as smart robotics, electronic skin, human motion, health-monitoring systems, and human–machine interactive systems. In addition, due to its capacity to detect subtle mechanical modification, improved durability, negligible hysteresis and large working window, many others applications could also envisage as advance monitoring techniques in plant health biology, individual/environment interaction and to monitor health infrastructures as already proposed by others groups.[74–76]

4. Experimental Section

Materials

Multi-walled carbon nanotubes (MWCNTs) are purchased from cheaptubes.com (purity of >95 wt%) with 8-15nm outer diameter and length of 10-50μm. Silver nanowires (Ag NWs) are purchased from Sigma Aldrich. The diameter and length of the NWs are 35 ±5nm and 25 ± 5μm, respectively. Dragon Skin™ silicones are used for a variety of applications, ranging from creating skin effects and other movie special effects to making production moulds for casting a variety of materials. Due to their superior physical properties and flexibility, they are also used for medical prosthetics and cushioning applications. It is purchased from Smooth-On company.

Synthesis of conductive solution and stretchable substrate using Dragon Skin™

MWCNTs/IPA solution: Mix CNTs in isopropanol (IPA) according to the desired weight ratio. The optimized weight percent is 0.5 wt%. Place the solution in ultrasonicator and let it for one hour to detangle the nanotubes to form uniform suspension.

Dragon Skin™: As a stretchable organic part, DS elastomer is made using part A and part B. The mass ratio between the two is 1:1. Then, this mixture is thoroughly mixed and degassed for 2 min in a desiccator. Following this step, an ≈1000 μm thick DS layer is drop casted over Kapton tape or SU-8 rigid pattern. The DS layer is kept at room temperature for 45 min to finish the curing process.

Functional characterization of the sensors

The electromechanical properties of the developed strain sensors are subsequently characterized using our custom-built test-bench set up. The change in resistance while stretching the DS substrate using a linear stage is monitored using LabVIEW controlled Keithley 2400 source meter. The linear stage is controlled using the E-861 PiezoWalk® NEXACT® Controller. The stretch rate was varied between 0.01 mm/s to 10 mm/s.

Supporting Information

Supporting Information is available from the Wiley Online Library or from the author.

Acknowledgements

This work was financially supported through EU H2020 SmartVista project, which has received funding from the European Union's Horizon 2020 research and innovation programme under the grant agreement No. 825114.

Conflict of interest

The authors declare no conflict of interest.

References

[1] J. C. Yang, J. Mun, S. Y. Kwon, S. Park, Z. Bao, S. Park, *Adv. Mater.* **2019**, *31*, 1.

[2] R. Dahiya, N. Yogeswaran, F. Liu, L. Manjakkal, E. Burdet, V. Hayward, H. Jorntell, *Proc. IEEE* **2019**, *107*, 2016.

[3] C. G. Núñez, W. T. Navaraj, E. O. Polat, R. Dahiya, *Adv. Funct. Mater.* **2017**, *27*, 1606287.

[4] Q. Luo, H. Ma, Q. Hou, Y. Li, J. Ren, X. Dai, Z. Yao, Y. Zhou, L. Xiang, H. Du, H. He, N. Wang, K. Jiang, H. Lin, H. Zhang, Z. Guo, *Adv. Funct. Mater.* **2018**, *28*, 1706777.

[5] Cai Jie, W. Xu, Y. Liu, Z. Zhu, G. Liu, W. Ding, G. Wang, H. Wang, Y. Luo, *Eng. Sci.* **2019**, *5*, 21.

[6] Hafez Ahmed M., J. Sheng, D. Cao, Y. Chen, H. Zhu, *ES Energy Environ.* **2019**, *5*, 85.

[7] A. Shankar, E. Salcedo, A. Berndt, D. Choi, J. E. Ryu, *Adv. Compos. Hybrid Mater.* **2018**, *1*, 193.

[8] A. S. Dahiya, J. Thireau, J. Boudaden, S. Lal, U. Gulzar, Y. Zhang, T. Gil, N. Azemard, P. Ramm, T. Kiessling, C. O\textquotesingleMurchu, F. Sebelius, J. Tilly, C. Glynn, S. Geary, C. O\textquotesingleDwyer, K. M. Razeeb, A. Lacampagne, B. Charlot, A. Todri-Sanial, *J. Electrochem. Soc.* **2020**, *167*, 37516.

[9] J. W. Jeong, Y. W. Jang, I. Lee, S. Shin, S. Kim, *IFMBE Proc.* **2009**, *25*, 282.

[10] P. Perego, C. Standoli, G. Andreoni, *Conf. Proc. Pap. – Sensors Appl.* **2015**.

[11] Y. Lee, W. Chung, *Sensors Actuators B. Chem.* **2009**, *140*, 390.

[12] Smart Autonomous Multi Modal Sensors for Vital Signs Monitoring. *EU Proj.* **2019**.

[13] G. H. Tison, J. M. Sanchez, B. Ballinger, A. Singh, J. E. Olgin, M. J. Pletcher, E. Vittinghoff, E. S. Lee, S. M. Fan, R. A. Gladstone, C. Mikell, N. Sohoni, J. Hsieh, G. M. Marcus, *JAMA Cardiol.* **2018**, *3*, 409.

[14] A. Kamiŝalić, I. Fister, M. Turkanović, S. Karakatiĉ, *Sensors (Switzerland)* **2018**, *18*.

[15] S. Hwang, S. H. Lee, *Autom. Constr.* **2017**, *83*, 330.

[16] R. López-Blanco, M. A. Velasco, A. Méndez-Guerrero, J. P. Romero, M. D. del Castillo, J. I. Serrano, E. Rocon, J. Benito-León, *J. Neurol. Sci.* **2019**, *401*, 37.

[17] N. Thomas, I. Lähdesmäki, B. A. Parviz, *Sensors Actuators, B Chem.* **2012**, *162*, 128.

[18] V. L. Alexeev, S. Das, D. N. Finegold, S. A. Asher, *Clin. Chem.* **2004**, *50*, 2353.

[19] W. March, D. Lazzaro, S. Rastogi, *Diabetes Technol. Ther.* **2006**, *8*, 312.

[20] M. Elsherif, M. U. Hassan, A. K. Yetisen, H. Butt, *ACS Nano* **2018**, *12*, 5452.

[21] J. Park, J. Kim, S.-Y. Kim, W. H. Cheong, J. Jang, Y.-G. Park, K. Na, Y.-T. Kim, J. H. Heo, C. Y. Lee, J. H. Lee, F. Bien, † Jang-Ung Park, *Sci. Adv.* **2018**, *4*, eaap9841.

[22] K. Takei, W. Gao, C. Wang, A. Javey, *Proc. IEEE* **2019**, 1.

[23] S. Han, C. Liu, H. Xu, D. Yao, K. Yan, H. Zheng, H. Chen, X. Gui, S. Chu, C. Liu, *npj*

Flex. Electron. **2018**, *2*, 16.

[24] A. Chhetry, M. Sharifuzzaman, H. Yoon, S. Sharma, X. Xuan, J. Y. Park, *ACS Appl. Mater. Interfaces* **2019**, *11*, 22531.

[25] A. Qiu, P. Li, Z. Yang, Y. Yao, I. Lee, J. Ma, *Adv. Funct. Mater.* **2019**, *29*, 1.

[26] W. Navaraj, R. Dahiya, *Adv. Intell. Syst.* **2019**, *1900051*, 1900051.

[27] Z. Pei, Y. Liu, Q. Zhang, D. Zhao, J. Wang, Z. Yuan, W. Zhang, S. Sang, *Adv. Electron. Mater.* **2019**, *1900227*, 1.

[28] H. Mai, R. Mutlu, C. Tawk, G. Alici, V. Sencadas, *Compos. Sci. Technol.* **2019**, *173*, 118.

[29] W. Dang, E. S. Hosseini, R. Dahiya, In *2018 IEEE SENSORS*; 2018; pp. 1–4.

[30] S. Khan, S. Tinku, L. Lorenzelli, R. S. Dahiya, *IEEE Sens. J.* **2015**, *15*, 3146.

[31] D. S. Kim, Y. J. Jeong, B. K. Lee, A. Shanmugasundaram, D. W. Lee, *Sensors Actuators, B Chem.* **2017**, *240*, 566.

[32] Y. H. Wen, G. Y. Yang, V. J. Bailey, G. Lin, W. C. Tang, J. H. Keyak, In *2005 3rd IEEE/EMBS Special Topic Conference on Microtechnology in Medicine and Biology*; 2005; Vol. 2005, pp. 302–304.

[33] D. Kang, P. V Pikhitsa, Y. W. Choi, C. Lee, S. S. Shin, L. Piao, B. Park, K. Suh, T. Kim, M. Choi, *Nature* **2014**, *516*, 222.

[34] T. Lee, Y. W. Choi, G. Lee, S. M. Kim, D. Kang, M. Choi, *RSC Adv.* **2017**, *7*, 34810.

[35] J. Chen, Q. Yu, X. Cui, M. Dong, J. Zhang, C. Wang, J. Fan, Y. Zhu, Z. Guo, *J. Mater. Chem. C* **2019**, *7*, 11710.

[36] J. Chen, Y. Zhu, J. Huang, J. Zhang, D. Pan, J. Zhou, J. E. Ryu, A. Umar, Z. Guo, *Polym. Rev.* **2020**.

[37] R. Yin, S. Yang, Q. Li, S. Zhang, H. Liu, J. Han, C. Liu, C. Shen, *Sci. Bull.* **2020**, *65*, 899.

[38] S. Zhang, K. Sun, H. Liu, X. Chen, Y. Zheng, X. Shi, D. Zhang, L. Mi, C. Liu, C. Shen, *Chem. Eng. J.* **2020**, *387*, 124045.

[39] X. Chen, H. Liu, Y. Zheng, Y. Zhai, X. Liu, C. Liu, L. Mi, Z. Guo, C. Shen, *ACS Appl. Mater. Interfaces* **2019**, *11*, 42594.

[40] P. C. Ma, N. A. Siddiqui, G. Marom, J. K. Kim, *Compos. Part A Appl. Sci. Manuf.* **2010**, *41*, 1345.

[41] R. Zhang, H. Deng, R. Valenca, J. Jin, Q. Fu, E. Bilotti, T. Peijs, *Compos. Sci. Technol.* **2013**, *74*, 1.

[42] J. Chen, H. Li, Q. Yu, Y. Hu, X. Cui, Y. Zhu, W. Jiang, *Compos. Sci. Technol.* **2018**, *168*, 388.

[43] H. Yang, X. Yao, L. Yuan, L. Gong, Y. Liu, *Nanoscale* **2019**, *11*, 578.

[44] Q. Li, H. Liu, S. Zhang, D. Zhang, X. Liu, Y. He, L. Mi, J. Zhang, C. Liu, C. Shen, Z. Guo, *ACS Appl. Mater. Interfaces* **2019**, *11*, 21904.

[45] H. Liu, Q. Li, Y. Bu, N. Zhang, C. Wang, C. Pan, L. Mi, Z. Guo, C. Liu, C. Shen, *Nano Energy* **2019**, *66*, 104143.

[46] D. Jiang, Y. Wang, B. Li, C. Sun, Z. Wu, H. Yan, L. Xing, S. Qi, Y. Li, H. Liu, W. Xie, X. Wang, T. Ding, Z. Guo, *Macromol. Mater. Eng.* **2019**, *304*, 1900074.

[47] S. Zhang, L. Cai, W. Li, J. Miao, T. Wang, J. Yeom, N. Sepúlveda, C. Wang, *Adv. Electron. Mater.* **2017**, *3*, 1700067.

[48] Huang Hailong, L. Han, Y. Wang, Z. Yang, F. Zhu, M. Xu, *Eng. Sci.* **2020**, *9*, 60.

[49] H. Gu, H. Zhang, C. Ma, H. Sun, C. Liu, K. Dai, J. Zhang, R. Wei, T. Ding, Z. Guo, *J. Mater. Chem. C* **2019**, *7*, 2353.

[50] Z. Wang, H. Li, H. Hu, Y. Fan, R. Fan, B. Li, J. Zhang, H. Liu, J. Fan, H. Hou, F. Dang, Z. Kou, Z. Guo, *Adv. Electron. Mater.* **2020**, *6*, 1901005.

[51] Z. Wang, K. Sun, P. Xie, Y. Liu, Q. Gu, R. Fan, *Compos. Sci. Technol.* **2020**, *188*, 107969.

[52] K. Sun, L. Wang, Z. Wang, X. Wu, G. Fan, Z. Wang, C. Cheng, R. Fan, M. Dong, Z. Guo, *Phys. Chem. Chem. Phys.* **2020**, *22*, 5114.

[53] K. Sun, J. Dong, Z. Wang, Z. Wang, G. Fan, Q. Hou, L. An, M. Dong, R. Fan, Z. Guo, *J. Phys. Chem. C* **2019**, *123*, 23635.

[54] P. Xie, Y. Li, Q. Hou, K. Sui, C. Liu, X. Fu, J. Zhang, V. Murugadoss, J. Fan, Y. Wang, R. Fan, Z. Guo, *J. Mater. Chem. C* **2020**, *8*, 3029.

[55] V. K. S. Shante, S. Kirkpatrick, *Adv. Phys.* **1971**, *20*, 325.

[56] M. Amjadi, A. Pichitpajongkit, S. Lee, S. Ryu, I. Park, *ACS Nano* **2014**, *8*, 5154.

[57] L. Xu, Y. Yang, Z.-W. Hu, S.-H. Yu, *ACS Nano* **2016**, *10*, 3823.

[58] K. Waseem, H. Nawaf, *Sci. Appl. Tailored Nanostructures* **2016**, 50.

[59] Kyun Kyu Kim, S. Hong, H. M. Cho, J. Lee, Y. D. Suh, J. Ham, S. H. Ko, *Nano Lett.* **2015**, *15*, 5240.

[60] J. T. Muth, D. M. Vogt, R. L. Truby, D. B. Kolesky, R. J. Wood, J. A. Lewis, *Adv. Mater.* **2014**, *26*, 6307.

[61] J. W. Boley, E. L. White, G. T. C. Chiu, R. K. Kramer, *Adv. Funct. Mater.* **2014**, *24*, 3501.

[62] M. Bhattacharjee, M. Soni, P. Escobedo, R. Dahiya, *Adv. Electron. Mater.* **2020**, 2000445.

[63] E. Kim, Y. Xia, G. M. Whitesides, *J. Am. Chem. Soc.* **1996**, *118*, 5722.

[64] B. Ha, S. Jo, *Sci. Rep.* **2017**, *7*, 1.

[65] M. Tanahashi, *Materials (Basel).* **2010**, *3*, 1593.

[66] T. S. Natarajan, S. B. Eshwaran, K. W. Stöckelhuber, S. Wießner, P. Pötschke, G. Heinrich, A. Das, *ACS Appl. Mater. Interfaces* **2017**, *9*, 4860.

[67] L. Jin, A. Chortos, F. Lian, E. Pop, C. Linder, Z. Bao, W. Cai, *Proc. Natl. Acad. Sci.*

U. S. A. **2018**, *115*, 1986.

[68] H. Zhang, W. Niu, S. Zhang, *ACS Appl. Mater. Interfaces* **2018**, *10*, 32640.

[69] Z. Zeng, S. I. Seyed Shahabadi, B. Che, Y. Zhang, C. Zhao, X. Lu, *Nanoscale* **2017**, *9*, 17396.

[70] D. J. Lipomi, M. Vosgueritchian, B. C. Tee, S. L. Hellstrom, J. A. Lee, C. H. Fox, Z. Bao, *Nat. Nanotechnol.* **2011**, *6*, 788.

[71] L. Duan, S. Fu, H. Deng, Q. Zhang, K. Wang, F. Chen, Q. Fu, *J. Mater. Chem. A* **2014**, *2*, 17085.

[72] T. Yamada, Y. Hayamizu, Y. Yamamoto, Y. Yomogida, A. Izadi-Najafabadi, D. N. Futaba, K. Hata, *Nat. Nanotechnol.* **2011**, *6*, 296.

[73] A. Todri-sanial, R. R. Pandey, J. Liang, Piezoelectric Biosensor **2019**.

[74] Y. Zhao, S. Gao, J. Zhu, J. Li, H. Xu, K. Xu, H. Cheng, X. Huang, *ACS Omega* **2019**, *4*, 9522.

[75] C. Tsogka, E. Daskalakis, G. Comanducci, F. Ubertini, *Comput. Civ. Infrastruct. Eng.* **2017**, *32*, 288.

[76] Y. Yang, Z. D. Deng, *Appl. Phys. Rev.* **2019**, *6*, 11309.

[77] J. Chen, Y. Zhu, W. Jiang, *Compos. Sci. Technol.* **2020**, *186*, 107938.

Figures

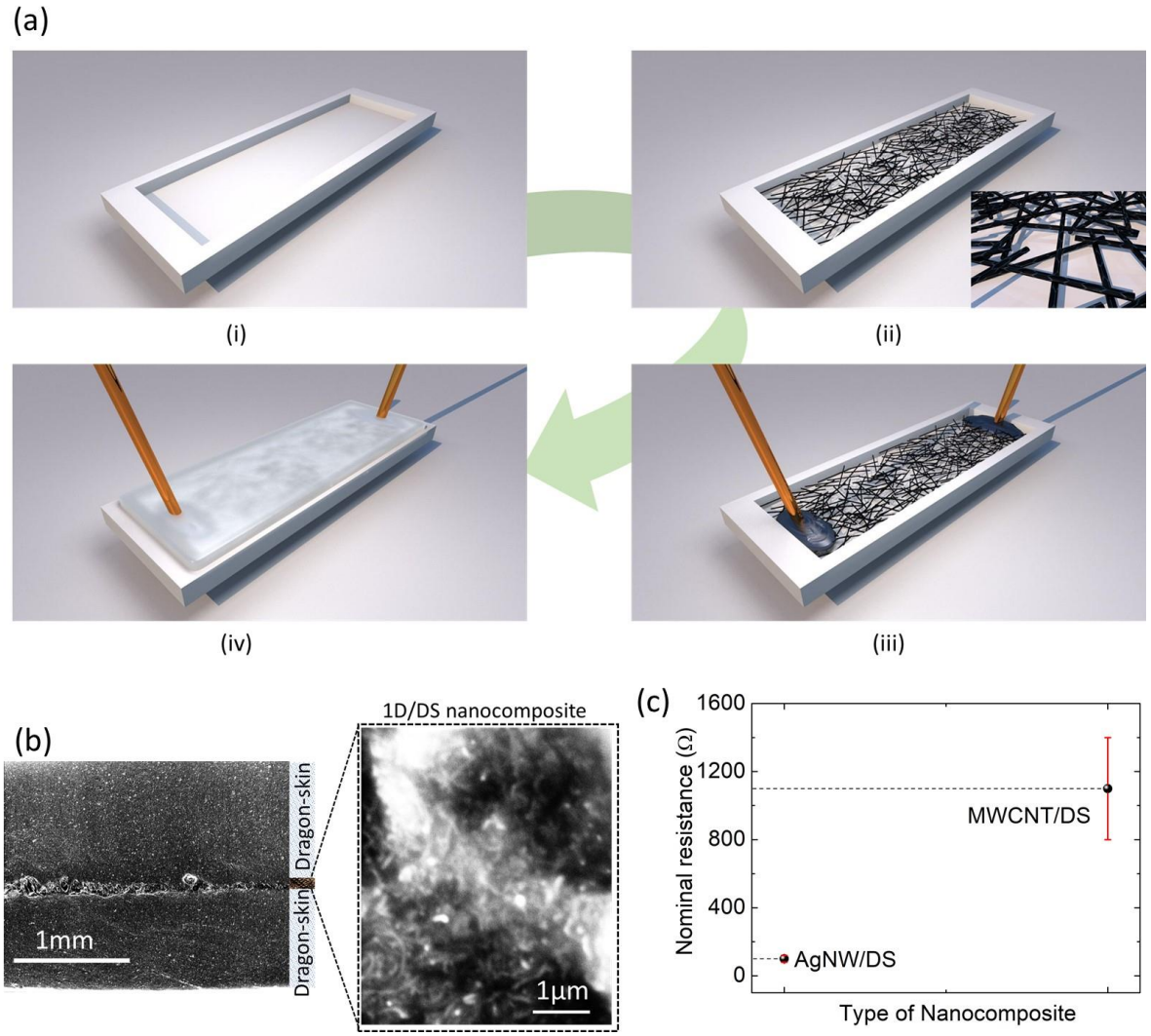

Figure 1. Schematic of the micromolding-in-capillary (MIMIC) fabrication process of the stretchable strain sensor, b) cross-sectional SEM images of the sensor illustrating network of nanotubes encapsulated in dragon-skin (DS) polymer, and c) average nominal device resistance of the multi-walled carbon nanotubes (MWCNTs) / DS and silver nanowires (Ag NWs) / DS nanocomposite materials.

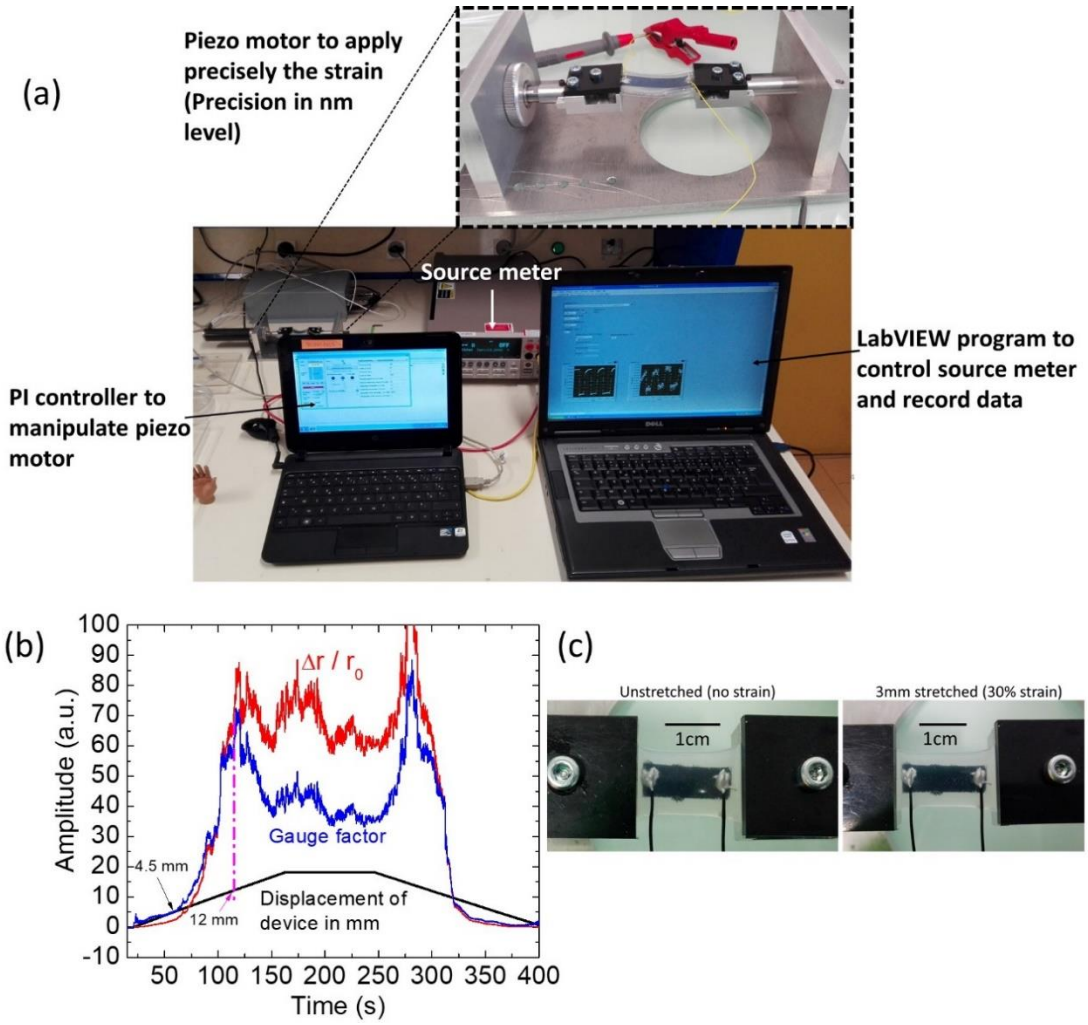

Figure 2: (a) Optical image of the custom-built test bench. Zoomed photo showing a sample mounted on a linear stage for the stretching test (b) electromechanical characterization of the MWCNT/DS sensor results: gauge factor and change in resistance as a function of displacement. The two arrows indicate limits of different regime of the sensor performance. The first one at 4.5mm of stretching for linear region limit and the second one at 12mm stretching for non-linear response limit. (c) optical image of the sensor during no stretching and 30% stretched.

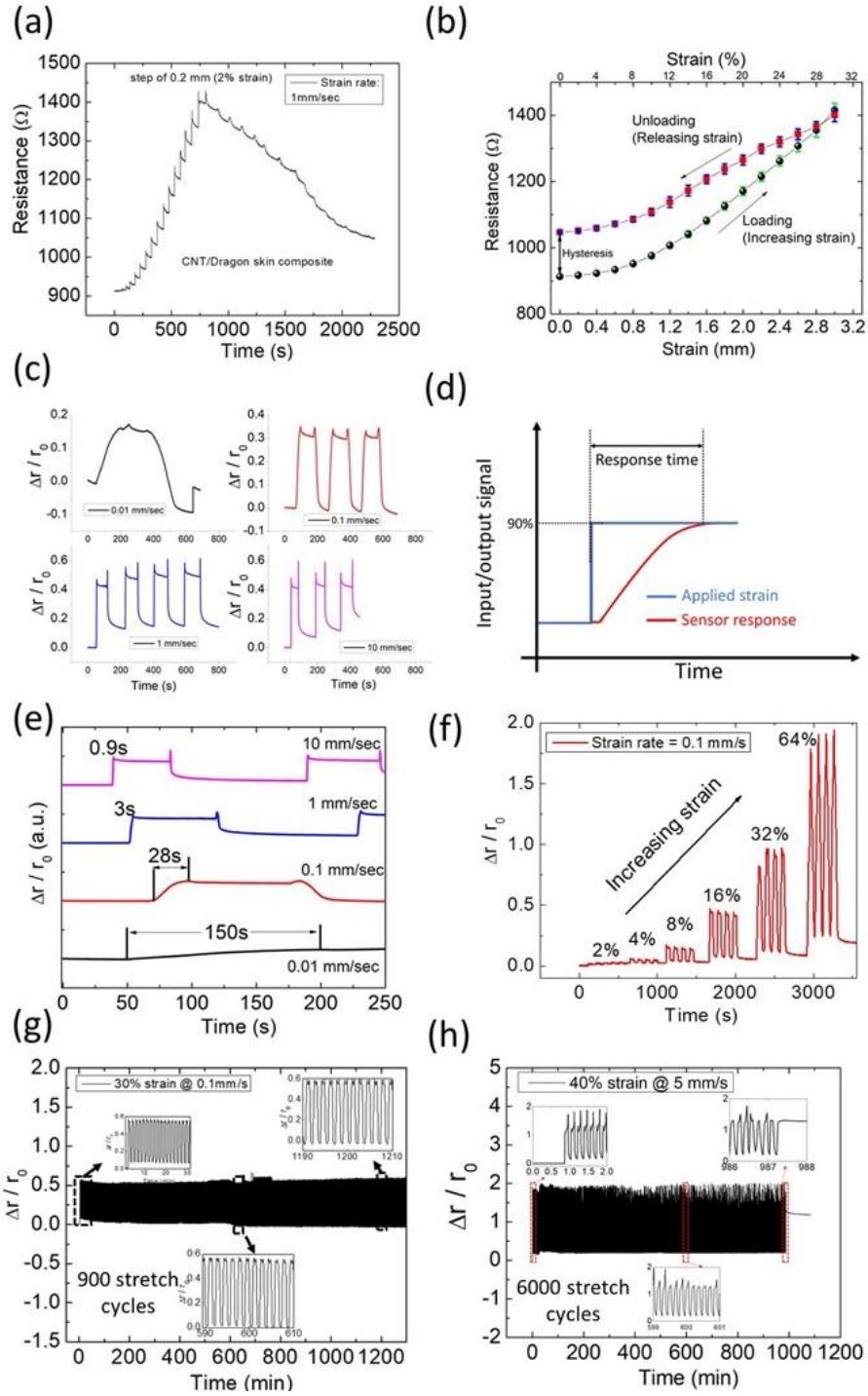

Figure 3: Electromechanical characterization of the MWCNT/DS nanocomposite-based sensor: (a) change in resistance plotted as a function of tensile strain with increasing step of 2%. (b) hysteresis of the device. (c) relative change in resistance when strained to 30% at different rate (0.01mm/s, 0.1mm/s, 1mm/s, and 10mm/s). (d) graphical representation of the response time of a typical strain sensor. (e) graph showing the response time when device strained to 30% at different rate. (f) relative change in resistance when strained from 2% to 64%. (g) Long-term stability of the sensor for 900 cycles when stretched to 30% at 0.1mm/s and (h) Long-term stability of the sensor for 6000 cycles when subjected to 40% strain at 5mm/s.

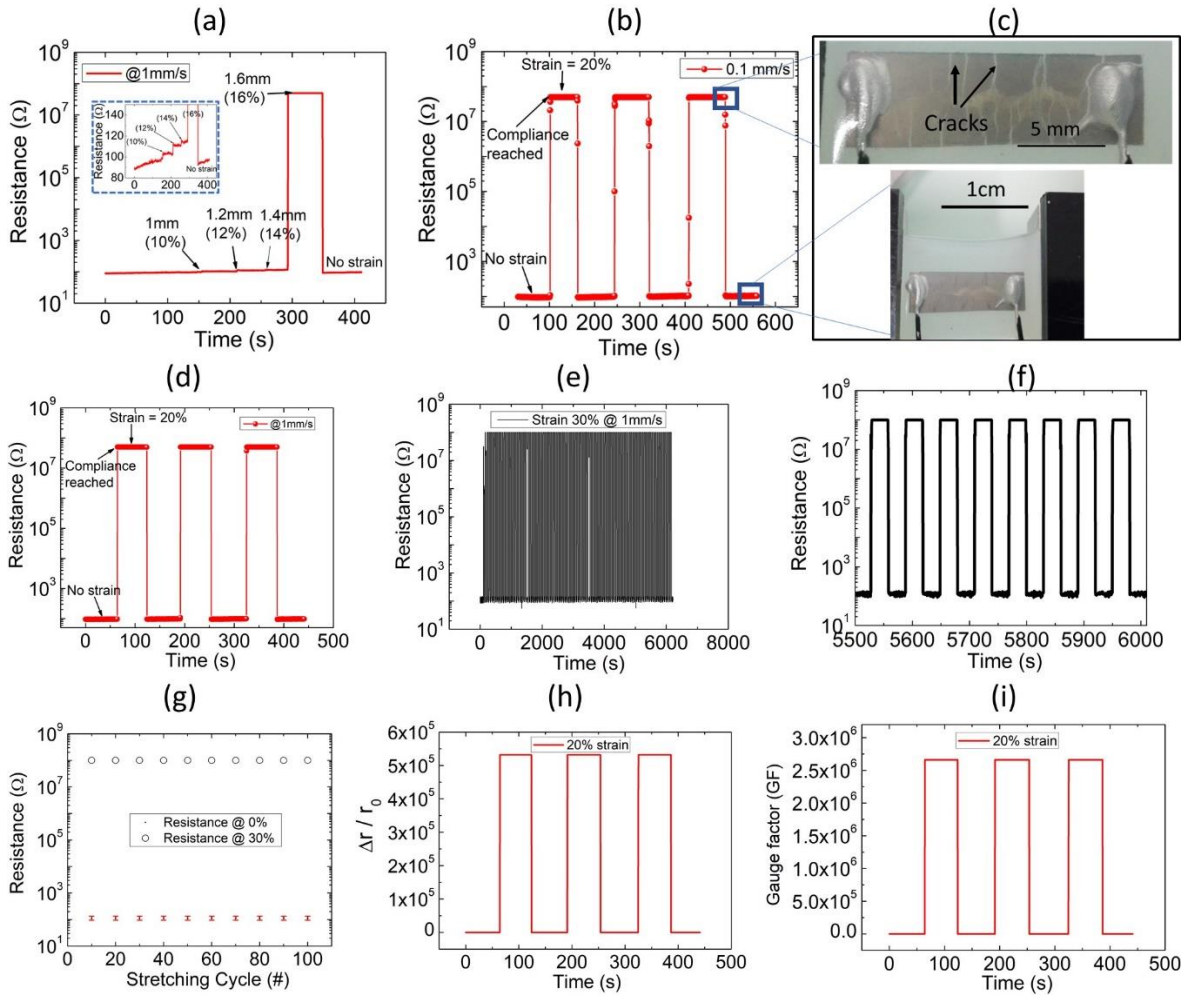

Figure 4: Electromechanical characterization of the AgNWs/DS nanocomposite-based sensor: a) change in resistance as a function of tensile strain. Inset shows the zoom of Fig. 4a. (b) time response of the device under repeated stretching with 20% strain and released back to 0% strain at 0.1mm/s. (c) optical images of the device when stretch to 20% and when released back to 0% strain. (d) time response of the device under repeated stretching with 20% strain and released back to 0% strain at 1mm/s strain rate. (e) Long-term stability of the sensor for 100 cycles. (f) Zoom of graph in panel 4e. (g) Resistance at 0% and 30% strain, extracted from graph shown in panel 4e. (h) relative change in resistance when strained to 20%. (i) Gauge factor of the device obtained at 20% stretching.

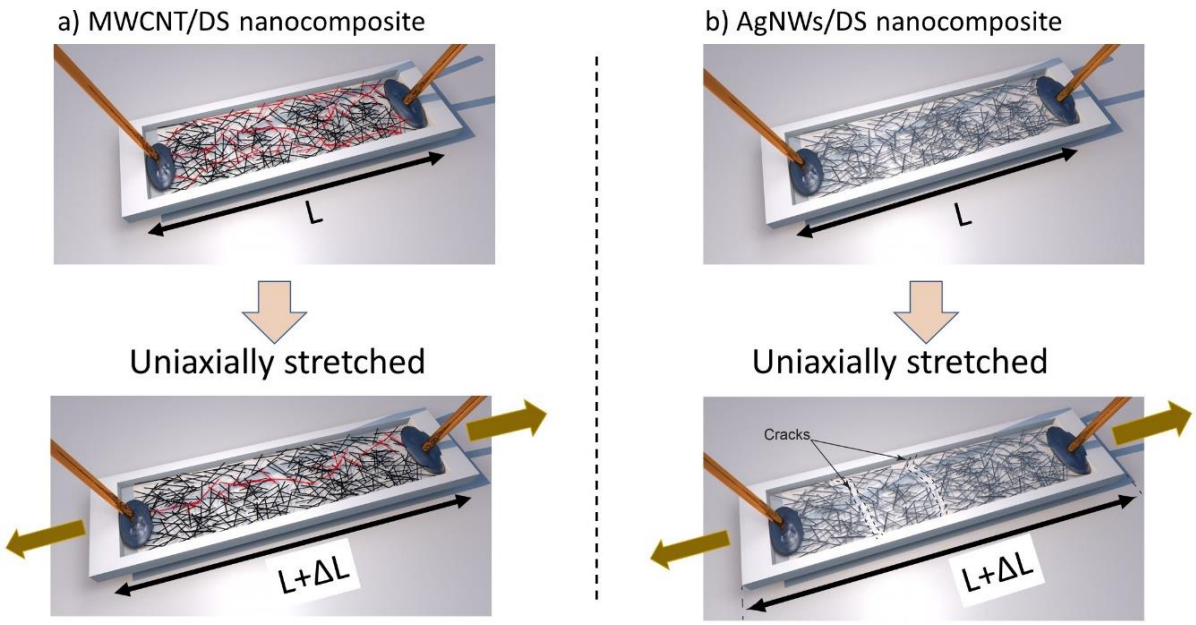

Figure 5: Schematic diagrams of the stretched and unstretched nanocomposites, illustrating the conducting mechanisms of the strain sensors: (a) MWCNT/DS composite and (b) AgNWs/DS composite.

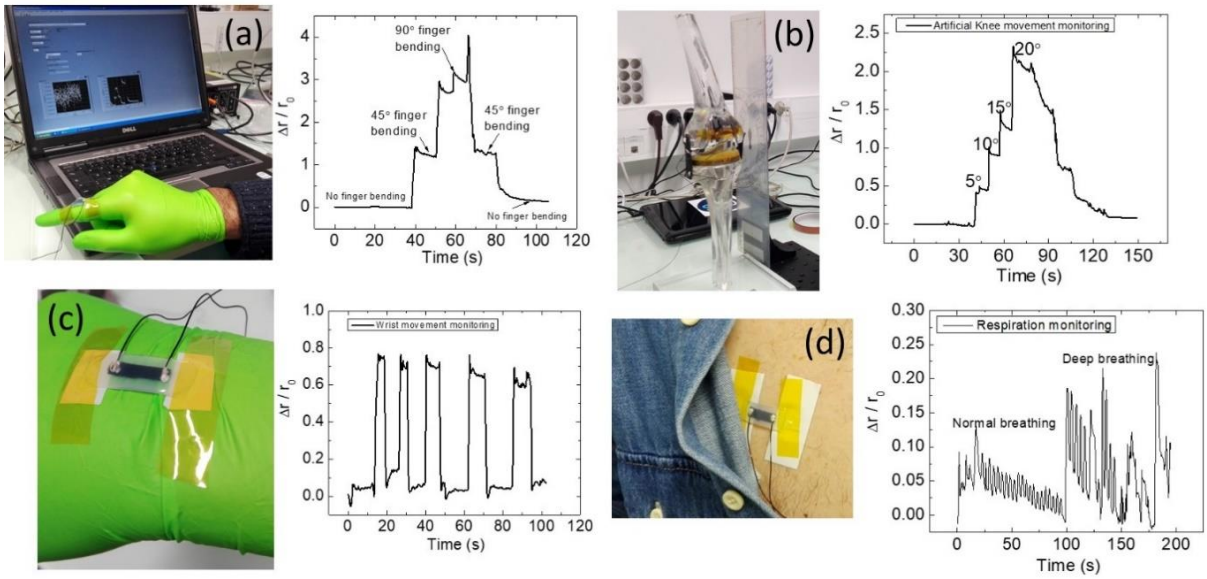

Figure 6: Illustration of the human activity monitoring using MWCNT/DS sensor: (a) photo showing the sample mounted on a glove used for the finger motion detection and measured electrical resistance from the sensor for three different states (no bending, 45°bended and 90° bended). (b) optical photo showing sensor placed on artificial knee model. Relative resistance responses of the strain sensor for detecting the bending state of a skeleton knee. (c) Detection of human wrist deformations by the strain sensor and optical photo. (d) Relative change in the sensor resistance during the respiration process when breathing rhythm is changed from normal to deep.

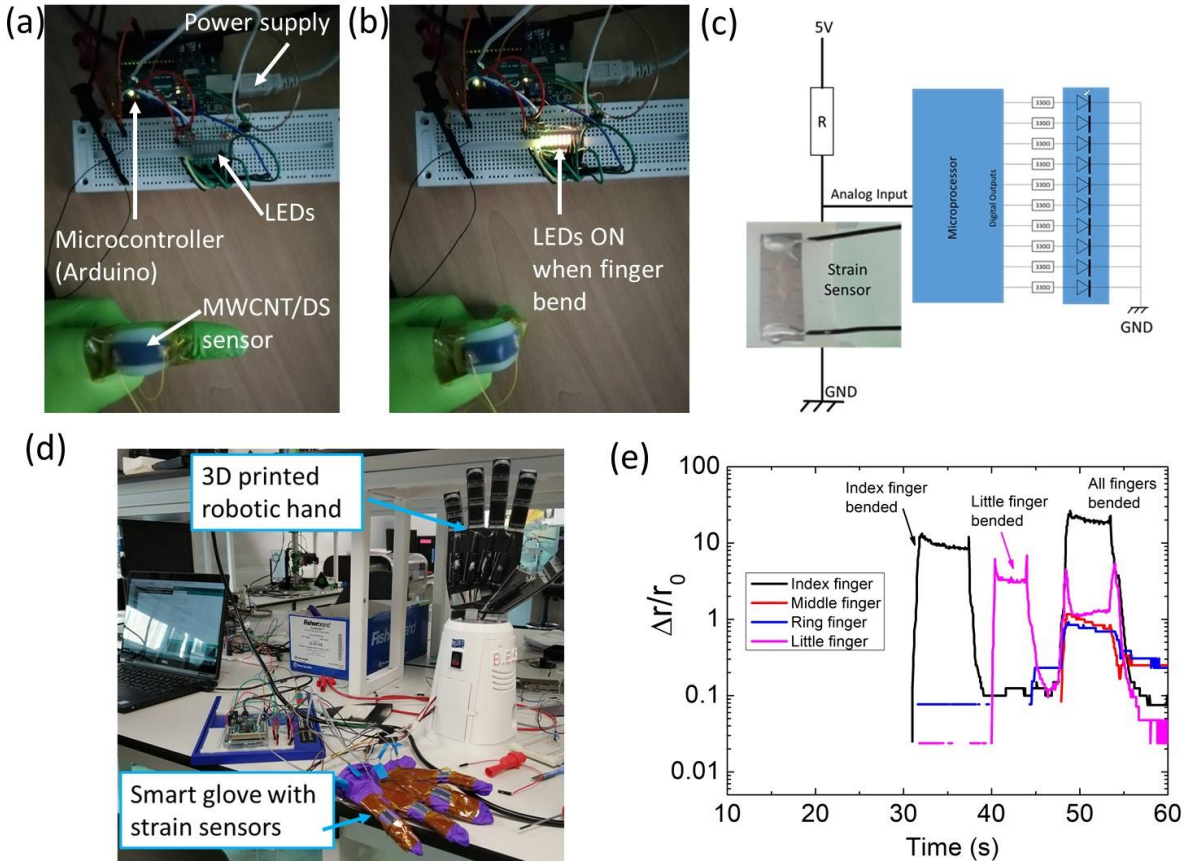

Figure 7: Illustration of finger movement monitoring with an integrated electronic system constructed using a microcontroller, LEDs and strain sensor placed on the index finger. (a) optical image showing LEDs 'off' when no strain is applied to the sensor (zero degree bending of the finger). (b) LEDs turn 'on' when strain is applied to sensor on 90° bending of the finger. (c) simplified circuit diagram to explain the working operation. (d) Optical image of the test-bench set-up for the MWCNT/DS strain sensors to be used as a control mechanism for teleoperation for robotic end-effectors. (e) Graph depicting the relative change in the resistance of the sensor while bending fingers.

Table 1. Performances comparison of stretchable strain sensor materials investigated.

Material	Strain rate	Linearity	Sensitivity (Gauge factor, GF)	Hysteresis (first loading-unloading cycle)	Response time (sec)	Robustness	Cost	Ref.
MWCNTs	0.01 (mm/s)	Linear up to 45% strain	3-60	Negligible	150	High	Low	This work
	0.1 (mm/s)	Linear up to 45% strain	3-60	Negligible	28	High		
	1 (mm/s)	Linear up to 45% strain	3-60	Low	3	High		
	10 (mm/s)	Linear up to 45% strain	3-60	High	0.9	High		
Ag NWs	0.1 (mm/s)	Non-linear	$1\text{-}10^6$	Negligible	2	Fair	Low	This work
	1 (mm/s)	Non-linear	$1\text{-}10^6$	Negligible	0.3	Fair		
Ag NWs	0.55 mm/s	Linear up to 40%	2–14	Negligible	0.2	No data	Medium	[56]
Platinum (Pt)	1mm/min	Non-linear	2000	Negligible	No data	Poor	High	[33]
Ag nanoparticles	No data	Non-linear	10^7	low	No data	Medium	Medium	[47]
CNT/graphene	0.5/min	Linear up to 25%	17.5	High	No data	High	Low	[43]
CNT-Ag	No data	Linear up to 40%	172	No data	No data	High	Medium	[27]
CNTs	10 mm/min	Linear up to 200%	No data	High	0.2	High	Low	[77]
Carbon fibers and Ag NWs	No data	Linear up to 60%	1.5	Negligible	No data	High	Low	[46]